

Cite this: *Chem. Sci.*, 2022, 13, 10461

All publication charges for this article have been paid for by the Royal Society of Chemistry

# Phase-engineered high-entropy metastable FCC $\text{Cu}_{2-y}\text{Ag}_y(\text{In}_x\text{Sn}_{1-x})\text{Se}_2\text{S}$ nanomaterials with high thermoelectric performance†

Wanjia Zhang,<sup>‡a</sup> Yue Lou,<sup>‡\*a</sup> Hongliang Dong,<sup>b</sup> Fanshi Wu,<sup>a</sup> Janak Tiwari,<sup>c</sup> Zhan Shi,<sup>id d</sup> Tianli Feng,<sup>id c</sup> Sokrates T. Pantelides<sup>id e</sup> and Biao Xu<sup>id \*a</sup>

Crystal-phase engineering to create metastable polymorphs is an effective and powerful way to modulate the physicochemical properties and functions of semiconductor materials, but it has been rarely explored in thermoelectrics due to concerns over thermal stability. Herein, we develop a combined colloidal synthesis and sintering route to prepare nanostructured solids through ligand retention. Nano-scale control over the unconventional cubic-phase is realized in a high-entropy  $\text{Cu}_{2-y}\text{Ag}_y(\text{In}_x\text{Sn}_{1-x})\text{Se}_2\text{S}$  ( $x = 0-0.25$ ,  $y = 0, 0.07, 0.13$ ) system by surface-ligand protection and size-driven phase stabilization. Different from the common monoclinic phase, the unconventional cubic-phase samples can optimize electrical and thermal properties through phase and entropy design. A high power factor ( $0.44 \text{ mW m}^{-1} \text{ K}^{-2}$ ), an ultralow thermal conductivity ( $0.25 \text{ W m}^{-1} \text{ K}^{-1}$ ) and a  $ZT$  value of 1.52 are achieved at 873 K for the cubic  $\text{Cu}_{1.87}\text{Ag}_{0.13}(\text{In}_{0.06}\text{Sn}_{0.94})\text{Se}_2\text{S}$  nanostructured sample. This study highlights a new method for the synthesis of metastable phase high-entropy materials and gives insights into stabilizing the metastable phase through ligand retention in other research communities.

Received 25th May 2022  
Accepted 12th August 2022

DOI: 10.1039/d2sc02915d

rsc.li/chemical-science

## 1. Introduction

Thermoelectric devices can directly convert waste heat into electrical power without hazardous emissions and moving parts and have become an attractive option for improving energy utilization in applications such as medical devices,<sup>1</sup> thermal management,<sup>2</sup> cooling<sup>3,4</sup> and thermocells.<sup>5</sup> In general, the

energy conversion efficiency of a thermoelectric material is determined by the figure of merit,  $ZT = S^2\sigma T/k_{\text{tot}}$ , where  $S$  is the Seebeck coefficient,  $\sigma$  is the electrical conductivity,  $k_{\text{tot}}$  is the total thermal conductivity, and  $T$  is the working temperature. In the past few decades, several strategies such as band convergence,<sup>6-9</sup> resonance level,<sup>10,11</sup> introducing defects,<sup>12,13</sup> and controlling grain size<sup>14,15</sup> have been successfully developed to increase  $ZT$ . So far, TE materials have been thoroughly investigated, including  $\text{SnSe}$ ,<sup>16</sup>  $\text{GeTe}$ ,<sup>17</sup> carbon hybrids,<sup>18</sup>  $\text{Cu}_2\text{Se}$ <sup>19</sup> and organic thermoelectrics.<sup>20</sup> However, strong coupling between  $S$ ,  $\sigma$ , and  $k_{\text{tot}}$  remains a formidable challenge for further optimization of thermoelectric performance.

Phase engineering focuses on the synthesis of unconventional phases, phase transformations and phase-based heterostructures. In particular, preparation of unconventional phases in nanomaterials through carefully regulating reaction kinetics and/or thermodynamics endows them with distinctive properties.<sup>21-24</sup> Meanwhile, this concept may also be developed in a coordinated way with other aspects, including composition, architecture, and dimensionality engineering, to realize a higher level of control over thermoelectric materials. Recently, high-entropy alloys (HEAs), in which multiple elements are utilized to occupy equivalent atomic sites resulting in increased configurational entropy, have provided a new means for improving the thermoelectric performance of materials.<sup>25-27</sup> Based on the core effects of HEAs, a synergy of band structure engineering and all-scale hierarchical microstructures is well realized.<sup>28-30</sup> However, the metastable-phase engineering of

<sup>a</sup>Department of Chemistry and Chemical Engineering, Nanjing University of Science and Technology, Nanjing, Jiangsu 210094, P. R. China. E-mail: louyue@njjust.edu.cn; xubiao@njjust.edu.cn

<sup>b</sup>Center for High Pressure Science and Technology Advanced Research, Shanghai 201203, China

<sup>c</sup>Department of Mechanical Engineering, The University of Utah, Salt Lake City, UT 84112, USA

<sup>d</sup>State Key Laboratory of Inorganic Synthesis and Preparative Chemistry, College of Chemistry, Jilin University, Changchun 130012, P. R. China

<sup>e</sup>Department of Physics and Astronomy and Department of Electrical and Computer Engineering, Vanderbilt University, Nashville, TN 37235, USA

† Electronic supplementary information (ESI) available: List of chemicals, preparation of  $\text{Cu}_2\text{SnSe}_3$ ,  $\text{Cu}_2\text{SnSe}_2\text{S}$ ,  $\text{Cu}_2\text{In}_x\text{Sn}_{1-x}\text{Se}_2\text{S}$ ,  $\text{Cu}_3\text{InSnSe}_3\text{S}_2$  and  $\text{Cu}_{2-y}\text{Ag}_y(\text{In}_{0.06}\text{Sn}_{0.94})\text{Se}_2\text{S}$  nanocrystals, spark plasma sintering, characterization, measurement of thermoelectric properties, DFT calculation, formation energy calculation, the calculation details of the Lorentz factor ( $L$ ) and density of states effective mass ( $m_d^*$ ) via the single parabolic band (SPB) model, the calculation details of heat capacity  $C_p$  via the Debye-3 Einstein model, crystal structure characterization, microstructure and composition, electronic and phononic band structures and thermoelectric properties. See <https://doi.org/10.1039/d2sc02915d>

‡ These two authors contributed equally.



high-entropy bulk thermoelectric materials remains a great challenge. According to the Gibbs free energy equation ( $G = H - TS$ , where  $T$  is temperature,  $S$  is entropy, and  $H$  is enthalpy), high mixing entropy at high temperature can effectively reduce the  $G$  of the alloy system and promote the formation of the solid solution phase of the alloy. Therefore, the traditional synthesis of high-entropy alloys mostly relies on the high temperature melting method, and metastable phases in high-entropy systems are hard to achieve.<sup>26</sup> In contrast, phase engineering of nanomaterials may avoid high temperatures and pressures, because the molar Gibbs energy, the molar entropy and the molar enthalpy increase as the particle size decreases.<sup>31–33</sup> In colloidal synthesis, the retained surface ligand can prevent grain growth and stabilize metastable phases through tuning the surface-related  $H$ . On the basis of this, phase engineering of high entropy nanomaterials can be well realized by changing the reaction conditions such as the stoichiometric ratio of precursor to surfactant, and sintering conditions. Therefore, developing ligand-retention synthetic strategies for preparation of high-entropy nanostructured solids is of great importance but still remains unexplored.

$\text{Cu}_2\text{SnSe}_3$  is a p-type semiconductor with a direct bandgap of 0.84 eV, which has attracted increasing attention in the thermoelectric community due to its compositionally tunable electronic structure and intrinsically low lattice thermal conductivity.<sup>34,35</sup> Previous studies have shown that the thermoelectric properties of  $\text{Cu}_2\text{SnSe}_3$  can be improved by modulation doping, synergistic alloying and nanostructuring with second phases.<sup>34–38</sup> For example, Li *et al.*<sup>34</sup> showed that (Ag, In)-codoping provides an effective solution to optimize the  $ZT$  of  $\text{Cu}_2\text{SnSe}_3$  to 1.42 at 823 K. Ming *et al.*<sup>35</sup> achieved a record high  $ZT$  of 1.51 at 858 K for  $\text{Cu}_2\text{Sn}_{0.82}\text{In}_{0.18}\text{Se}_{2.7}\text{S}_{0.3}$  *via* alloying S and

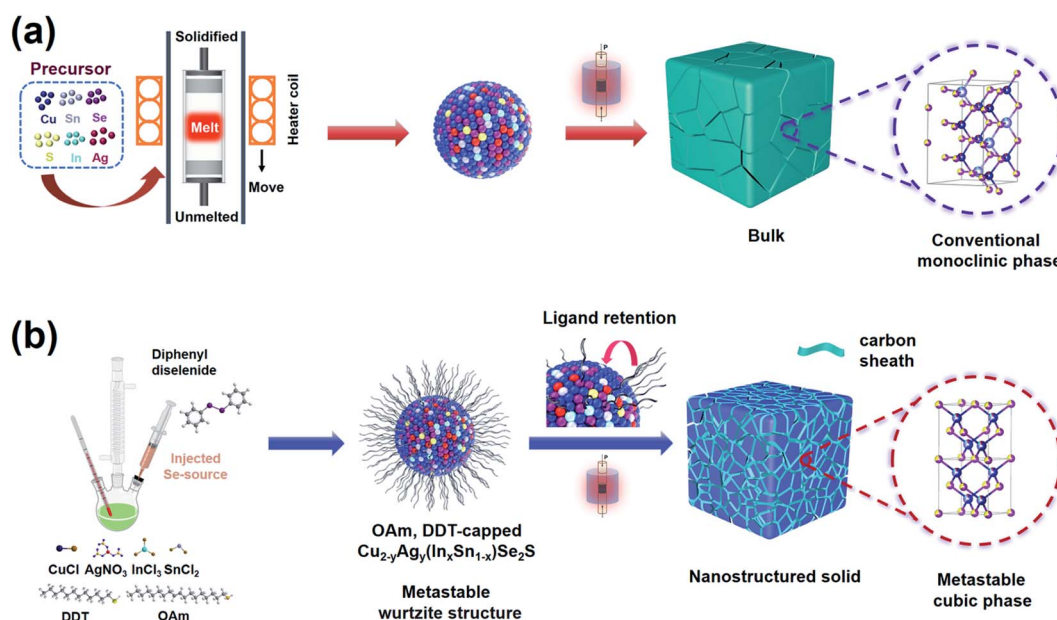
doping In. However, the structures of these materials are mostly monoclinic, while the cubic structure with high symmetry as a metastable phase is rarely obtained, as it requires thermodynamic control through specific synthetic conditions.

In this work, as shown in Scheme 1, we firstly adopt colloidal synthesis, performed at a low temperature for short reaction times, to obtain metastable wurtzite  $\text{Cu}_{2-y}\text{Ag}_y(\text{In}_x\text{Sn}_{1-x})\text{Se}_2\text{S}$  nanocrystals. Different from the monoclinic bulk materials in most of the literature,<sup>34–36,39–42</sup> a series of multinary chalcogenide nanostructured solids with a metastable cubic phase are obtained after spark plasma sintering (SPS). Here, oleylamine (OAm) and dodecanethiol (DDT) coated on nanoparticle surfaces could carbonize to protective amorphous carbon shells that can restrict the growth of nanoparticles and stabilize a metastable cubic phase of nanostructured solids. As a result, the cubic-phase, high-entropy  $\text{Cu}_{1.87}\text{Ag}_{0.13}(\text{In}_{0.06}\text{Sn}_{0.94})\text{Se}_2\text{S}$  nanomaterial achieves a high power factor (PF) of  $0.44 \text{ mW m}^{-1} \text{ K}^{-2}$ , an ultralow thermal conductivity of  $0.25 \text{ W m}^{-1} \text{ K}^{-1}$ , and a peak  $ZT$  of 1.52 at 873 K.

## 2. Results and discussion

### 2.1 Phase engineering through surface-ligand protection

$\text{Cu}_2\text{SnSe}_3$ ,  $\text{Cu}_2\text{SnSe}_2\text{S}$ ,  $\text{Cu}_2\text{In}_x\text{Sn}_{1-x}\text{Se}_2\text{S}$  ( $x = 0.05–0.4$ ),  $\text{Cu}_3\text{-InSnSe}_3\text{S}_2$ , and  $\text{Cu}_{2-y}\text{Ag}_y(\text{In}_{0.06}\text{Sn}_{0.94})\text{Se}_2\text{S}$  ( $y = 0, 0.07, 0.13$ ) nanocrystals were synthesized by the reaction of metal chlorides and diphenyl diselenide/DDT/OAm solution as the precursors (see the Experimental section in the ESI† for details). X-ray diffraction (XRD) patterns (Fig. S1a†) suggest that the as-synthesized nanocrystals have a wurtzite structure derived from ZnSe, in which the cationic  $\text{Zn}^{2+}$  ions are substituted by  $\text{Cu}^+$ ,  $\text{In}^{3+}$ , and  $\text{Sn}^{4+}$ , and anionic  $\text{Se}^{2-}$  ions are partly substituted



**Scheme 1** (a) The monoclinic  $\text{Cu}_2\text{SnSe}_3$ -based bulk materials reported in most of the literature<sup>34–36,39–42</sup> are obtained *via* the high temperature melting method. (b) Synthetic methods of the metastable wurtzite structure  $\text{Cu}_{2-y}\text{Ag}_y(\text{In}_x\text{Sn}_{1-x})\text{Se}_2\text{S}$  nanocrystals and metastable cubic  $\text{Cu}_{2-y}\text{Ag}_y(\text{In}_x\text{Sn}_{1-x})\text{Se}_2\text{S}$  nanostructured solids.



by  $S^{2-}$ .<sup>43</sup> As a representative, the powder XRD pattern of  $Cu_3$ - $InSnSe_3S_2$  nanocrystals was analyzed by the Rietveld refinement method (Fig. S1b†), in which the crystal structure fitted well to the wurtzite structure with space group  $P6_3mc$  (186) and the lattice parameters are listed in Table S1.† When Ag element is alloyed in  $Cu_{2-y}Ag_y(In_{0.06}Sn_{0.94})Se_2S$  ( $y = 0.07$  and  $0.13$ ), a small fraction of the second phase,  $CuAgS$ , is observed in the samples (Fig. S1a†). To characterize the thermoelectric properties of the dense materials compacted from these nanoparticles, the purified nanocrystals were sintered by SPS and characterized by XRD, as shown in Fig. 1a. The main peaks of SPSed- $Cu_2SnSe_3$  match well with the cubic phase  $Cu_2SnSe_3$  (PDF# 65-4145). The peaks shift to high angle after alloying S into the anionic site and/or doping In into the cationic site, indicating the shrinkage of lattice parameters. Interestingly, when the amount of indium increases to a certain amount, SPSed- $Cu_2In_{0.4}Sn_{0.6}Se_2S$  and SPSed- $Cu_3InSnSe_3S_2$  nanostructured solids have a tetragonal structure (space group  $I42m$ ) without impurities, and this tetragonal unit cell can be approximately depicted as a  $1 \times 1 \times 2$  supercell of cubic  $Cu_2SnSe_3$  (Fig. 1a and Table S1†). After Ag alloying, SPSed- $Cu_{1.93}Ag_{0.07}(In_{0.06}Sn_{0.94})Se_2S$  shows a cubic structure (Fig. 1c). Due to the larger ionic radius of  $Ag^+$  (1.26 Å) compared to that of  $Cu^+$  (0.96 Å), the diffraction peaks shift toward the low-angle direction with respect to cubic SPSed-

$Cu_2In_{0.06}Sn_{0.94}Se_2S$  (Fig. 1a) due to an expansion of the lattice. The cubic  $Cu_{1.8}Se$  phase still exists as a second phase in samples and disappears upon increasing In content and/or alloying Ag. In addition, according to the classical theory of grain growth,<sup>44</sup> the Zener pinning effect caused by the introduction of a second phase could inhibit grain growth to some extent.

From a synthetic perspective, a high-entropy system,  $Cu_{2-y}Ag_y(In_xSn_{1-x})Se_2S$  ( $x = 0-0.25$ ,  $y = 0, 0.07, 0.13$ ), with two metastable phases (wurtzite nanocrystals and cubic nanostructured solids) is obtained, which is hard to realize in their bulk counterparts. Formation energies of the cubic and monoclinic-phase  $Cu_2SnSe_3$ ,  $Cu_2SnSe_2S$ ,  $Cu_2In_{0.06}Sn_{0.94}Se_2S$ , and  $Cu_{1.87}Ag_{0.13}(In_{0.06}Sn_{0.94})Se_2S$ , and tetragonal-phase  $Cu_3$ - $InSnSe_3S_2$  are calculated by density functional theory (DFT). Indeed, all monoclinic crystals show lower formation energy than the metastable cubic phase (Table S2†). The colloidal synthetic strategy for monodisperse multinary chalcogenide nanocrystals and the following SPS process are the key factors for the retention of the metastable phase. As shown in Fig. 1f, FTIR spectrometry was performed to verify the surface ligand of OAm in a solution-synthesized  $Cu_{1.87}Ag_{0.13}(In_{0.06}Sn_{0.94})Se_2S$  sample. The presence of the OAm molecule is indicated by the symmetric and asymmetric stretching vibrations of  $-NH_2$  at  $3430.74\text{ cm}^{-1}$ , the bending vibrations of  $C=C$  and  $-NH_2$  bonds

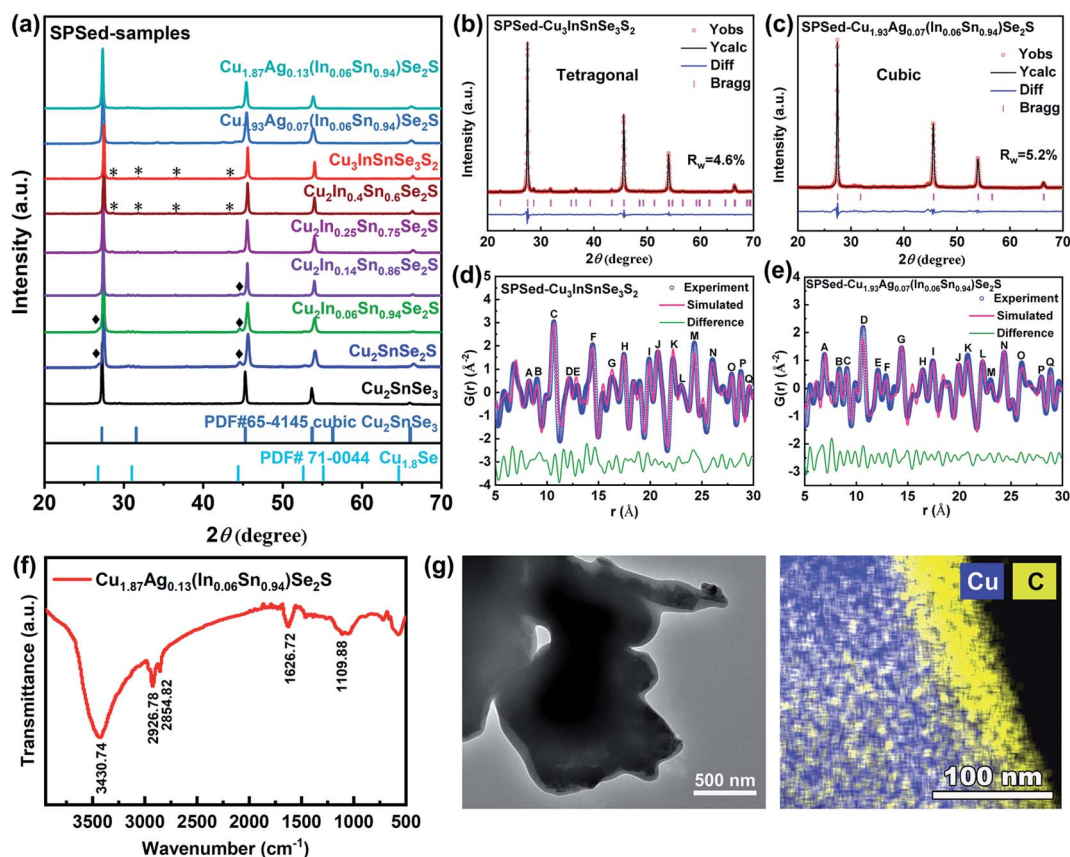


Fig. 1 (a) Powder X-ray diffraction (PXRD) patterns of the SPSed-samples. Rietveld refinement results of (b) SPSed- $Cu_3InSnSe_3S_2$  and (c) SPSed- $Cu_{1.93}Ag_{0.07}(In_{0.06}Sn_{0.94})Se_2S$ . PDF fit to the  $G(r)$  function in the range of 5–30 Å using the tetragonal model for (d) SPSed- $Cu_3InSnSe_3S_2$  and cubic model for (e) SPSed- $Cu_{1.93}Ag_{0.07}(In_{0.06}Sn_{0.94})Se_2S$ . (f) FTIR spectrum of solution-synthesized  $Cu_{1.87}Ag_{0.13}(In_{0.06}Sn_{0.94})Se_2S$ . (g) TEM image and EDS element map of Cu and C for SPSed- $Cu_{1.87}Ag_{0.13}(In_{0.06}Sn_{0.94})Se_2S$ .



at  $1626.72\text{ cm}^{-1}$ , and the bending vibration of the C–N bond at  $1109.88\text{ cm}^{-1}$ . During the nanocrystal consolidation process, OAm as a surfactant capping agent at the surface of colloidal nanoparticles can decrease the surface free energy of nanocrystals, simultaneously acting as a controllable molecular solder,<sup>45</sup> which might have a dominant effect that restricts the growth of nanoparticles and stabilizes the metastable phase.<sup>46–49</sup> Detailed evidence is shown in SEM and TEM images (Fig. 6b and c, and S9a and b†), and the EDS element map of SPSed-Cu<sub>1.87</sub>Ag<sub>0.13</sub>(In<sub>0.06</sub>Sn<sub>0.94</sub>)Se<sub>2</sub>S confirms the existence of carbon after sintering (Fig. 1g). In addition, the contents of hydrogen (0.05 wt%) and carbon (1.15 wt%) were measured in the SPSed-Cu<sub>1.87</sub>Ag<sub>0.13</sub>(In<sub>0.06</sub>Sn<sub>0.94</sub>)Se<sub>2</sub>S sample, and the results indicate that some of the surface ligands were converted into a mixture of organic hydrocarbons between nanograins of nanostructured solids during the sintering process (Fig. S9c†). Based on size reduction, metastable cubic nanostructured solids Cu<sub>2</sub>SnSe<sub>3</sub> and Cu<sub>2–y</sub>Ag<sub>y</sub>(In<sub>x</sub>Sn<sub>1–x</sub>)Se<sub>2</sub>S ( $x = 0–0.25$ ,  $y = 0, 0.07, 0.13$ ) compacted from the corresponding nanoparticles are obtained, which are different from the conventional monoclinic (space group *Cc*) structure of bulk Cu<sub>2</sub>SnSe<sub>3</sub>-based materials.<sup>34–36,39–42</sup> In addition, the successful synthesis of Cu<sub>2</sub>SnSe<sub>3</sub> and Cu<sub>2</sub>SnSe<sub>2</sub>S cubic nanostructured solids with low configuration entropy provides strong evidence that the metastable cubic phase does not originate from entropy effects, which is different from the strategy for stabilizing the cubic structure by entropy optimization in previous papers.<sup>25–27</sup>

In order to understand the local and long-range structures of the as-obtained nanostructured solids, an X-ray pair distribution function (X-PDF) analysis was performed. The corresponding Rietveld results are shown in Fig. 1d and e, and S1d and e.† It is evident that the global X-PDF structures of simulated structure models provide good descriptions of all the samples, demonstrating the overall crystallographic structure. The peaks with chemical bonding information in the diagrams labeled by letters can be well assigned to the atomic pair distances of the samples (Table S3†). As shown in Fig. 1e and S1e,† the residual curve (green curve) of the cubic model establishes much smoother characteristics in the large range from 10 Å to 30 Å, demonstrating long-range highly crystalline structures. In contrast, the local bonding interactions (5–10 Å) deviate significantly from the simulated profile for the cubic model, as observed from the asymmetric peaks and large fluctuations in the green line. Such a phenomenon is an indication of the local structural distortion with the unbalanced long and short bond lengths. The coexistence of the high-symmetry long-range structure and distorted local structure could be an example of ideal thermoelectric materials based on the 'phonon-glass, electron-crystal' concept that could lead to high electrical conductivity and low thermal conductivity and finally achieve a high *ZT* value.<sup>50,51</sup>

## 2.2 Microstructure and composition

The microstructures of the as-synthesized samples were comprehensively characterized. First, the hexagonal (wurtzite) structure of Cu<sub>2</sub>SnSe<sub>3</sub> is confirmed with an average size of

around 30 ( $\pm 10$ ) nm by transmission electron microscopy (TEM) (Fig. S3a and b†). Then, thiol is added to the reaction system as the S source and surfactant capping agent, which can passivate the crystalline facets of the wurtzite nanocrystals, and thus realize size control. As a result, the synthesized Cu<sub>2</sub>SnSe<sub>2</sub>S and Cu<sub>3</sub>InSnSe<sub>3</sub>S<sub>2</sub> nanocrystals show hexagonal structures with an average size of 10 ( $\pm 2$ ) nm (Fig. S4a and b and S5a†). Elemental mapping measurement was performed to identify the presence of Cu, Ag, In, Sn, Se, and S elements in nanoparticles of Cu<sub>2</sub>SnSe<sub>3</sub>, Cu<sub>2</sub>SnSe<sub>2</sub>S, SPSed-Cu<sub>2</sub>SnSe<sub>3</sub>, SPSed-Cu<sub>2</sub>SnSe<sub>2</sub>S, and SPSed-Cu<sub>1.87</sub>Ag<sub>0.13</sub>(In<sub>0.06</sub>Sn<sub>0.94</sub>)Se<sub>2</sub>S. All elements in the samples show homogeneous distributions, and no significant local element enrichment is observed (Fig. S3c, S4c, S6b, S7b and S11d†). For nanostructured solids, Fig. S9a and b† show the scanning electron microscopy (SEM) surface micrographs of SPSed-Cu<sub>2</sub>In<sub>0.06</sub>Sn<sub>0.94</sub>Se<sub>2</sub>S and SPSed-Cu<sub>1.87</sub>Ag<sub>0.13</sub>(In<sub>0.06</sub>Sn<sub>0.94</sub>)Se<sub>2</sub>S pellets. A slight grain growth of nanoparticles can be observed during the sintering process and the final average grain sizes are 63.06 ( $\pm 30$ ) and 131.98 ( $\pm 50$ ) nm for SPSed-Cu<sub>2</sub>In<sub>0.06</sub>Sn<sub>0.94</sub>Se<sub>2</sub>S and SPSed-Cu<sub>1.87</sub>Ag<sub>0.13</sub>(In<sub>0.06</sub>Sn<sub>0.94</sub>)Se<sub>2</sub>S, respectively. Fig. S10a and d and S11a† show the high-resolution TEM (HRTEM) images of the SPSed-Cu<sub>2</sub>SnSe<sub>3</sub>, SPSed-Cu<sub>2</sub>SnSe<sub>2</sub>S, and SPSed-Cu<sub>1.87</sub>Ag<sub>0.13</sub>(In<sub>0.06</sub>Sn<sub>0.94</sub>)Se<sub>2</sub>S samples. The inverse fast Fourier transform (IFFT) images (Fig. S10b and e and S11b†) clearly show the highly dense dislocation arrays. In order to investigate the strain fields from distorted lattices caused by the strong mismatch of the atomic radius, geometric phase analysis (GPA) was performed based on IFFT images to calculate the strains. As shown in Fig. S10c and f and S11c,† strong strain distribution fluctuations can be observed in the SPSed samples, which should strongly affect the thermal transport process.

To further verify the single-phase and high-entropy configuration in the as-synthesized Cu<sub>3</sub>InSnSe<sub>3</sub>S<sub>2</sub> and SPSed-Cu<sub>3</sub>InSnSe<sub>3</sub>S<sub>2</sub>, high-angle annular dark-field scanning transmission electron microscopy (HAADF-STEM) was conducted. Fig. 2a and e show the HAADF-STEM images of a Cu<sub>3</sub>InSnSe<sub>3</sub>S<sub>2</sub> nanoparticle and SPSed-Cu<sub>3</sub>InSnSe<sub>3</sub>S<sub>2</sub> nanostructured solid viewed along the [001] and [110] zone axes, respectively. The atomic models of the hexagonal structure and tetragonal structure are in good agreement with the experimental images, indicating the consistency of the atomic lattices and positions of all atoms (Fig. 2b and f). As shown in Fig. 2d, all elements are distributed in the nanoparticle, and Cu and S are a little bit aggregated in the center of the particle. From our results and some literature reports,<sup>52,53</sup> we believe that the copper thiolate in solution could preferentially decompose into a Cu<sub>2–x</sub>S crystal nucleus due to its higher reactivity. Then highly active diphenyl diselenide (PhSeSePh) rapidly decomposes at high temperatures after injection and triggers the growth of nanocrystals, in which Se, Sn and In atoms gradually diffuse into the Cu<sub>2–x</sub>S crystal nucleus simultaneously with the epitaxial growth and maturation process. Therefore, enrichment of Cu and S elements in the middle of individual nanoparticles can be attributed to the preferential nucleation process of 1-dodecanethiol (both as a ligand and sulfur source) in the precursor solution and Cu before the injection of Se sources. As shown in Fig. 2h and S8,†



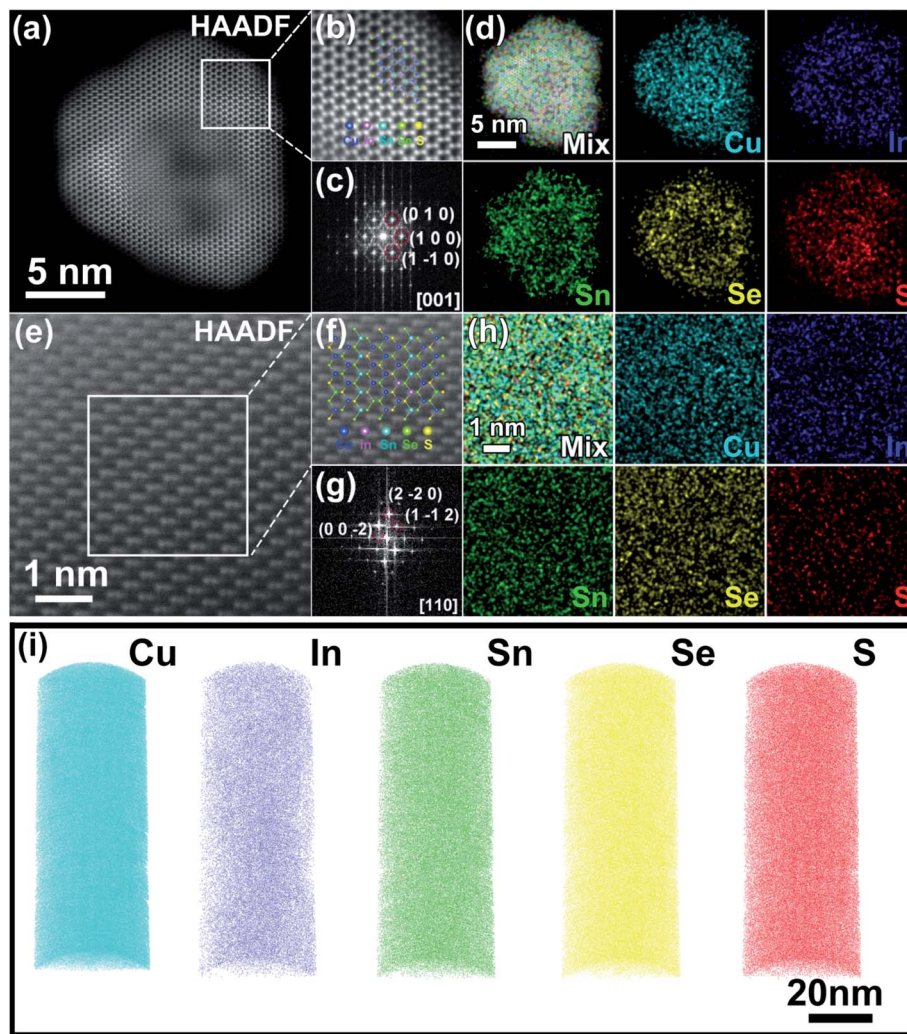


Fig. 2 Atomic structure recognition of solution-synthesized and SPSed- $\text{Cu}_3\text{InSnSe}_3\text{S}_2$ . (a) Atomic-resolution HAADF-STEM image, (b) atomic model, (c) corresponding FFT along the [001] zone axis and (d) EDS mapping of the as-synthesized  $\text{Cu}_3\text{InSnSe}_3\text{S}_2$  nanoparticle. (e) Atomic-resolution HAADF-STEM image, (f) atomic model, (g) corresponding FFT along the [110] zone axis and (h) EDS mapping of the SPSed- $\text{Cu}_3\text{InSnSe}_3\text{S}_2$  sample. (i) 3D-APT images showing the elemental distribution and multicomponent nature in the SPSed- $\text{Cu}_2\text{In}_{0.09}\text{Sn}_{0.91}\text{Se}_2\text{S}$ .

the EDS mapping of the SPSed- $\text{Cu}_3\text{InSnSe}_3\text{S}_2$  sample demonstrates that the distribution of all elements is homogeneous in the nanostructured solid.

Atom probe tomography (APT) analysis provides the mapping of three-dimensional microstructural and compositional information with sub-nanometer spatial accuracy and elemental sensitivity in the range of tens of ppm,<sup>54</sup> which can provide solid evidence that these elements are indeed homogeneously distributed in the nanostructured solid at the atomic scale. The 3D atomic maps and the nearest-neighbor (NN) atomic distribution of SPSed- $\text{Cu}_2\text{In}_{0.09}\text{Sn}_{0.91}\text{Se}_2\text{S}$  are shown in Fig. 2i and S14,<sup>†</sup> respectively. The measured NN atomic distance histograms of each element completely overlap with the calculated curves (Fig. S14<sup>†</sup>) without deviating from the randomized Gaussian peak, revealing the homogeneous distribution of the Cu, In, Sn, Se, and S elements. The homogeneous and disordered distribution of all the elements on the

macroscale, nanoscale, and atomic-scale confirms that the as-synthesized nanostructured solid is a high-entropy multinary metal chalcogenide.

### 2.3 Electronic and phononic band structures

To gain insight into the evolution of electronic states in the conventional monoclinic structure and metastable cubic structure, DFT calculations were performed. Fig. 3a and b show the electronic band structures of monoclinic and cubic  $\text{Cu}_{1.87}\text{Ag}_{0.13}(\text{In}_{0.06}\text{Sn}_{0.94})\text{Se}_2\text{S}$ , respectively. Those of  $\text{Cu}_2\text{SnSe}_3$ ,  $\text{Cu}_2\text{SnSe}_2\text{S}$ , and  $\text{Cu}_2\text{In}_{0.06}\text{Sn}_{0.94}\text{Se}_2\text{S}$  are shown in Fig. S15.<sup>†</sup> The monoclinic and cubic  $\text{Cu}_2\text{SnSe}_3$  are direct-band-gap semiconductors with band gaps ( $E_g$ ) of 0.12 and 0.11 eV, respectively (Fig. S15a and b<sup>†</sup>).  $E_g$  can be effectively enlarged by alloying S into the anionic site of  $\text{Cu}_2\text{SnSe}_3$  (Fig. S15c and d<sup>†</sup>). In-Doped  $\text{Cu}_2\text{SnSe}_2\text{S}$  pushes the Fermi level ( $E_f$ ) deep into the multiple bands and turns  $\text{Cu}_2\text{In}_{0.06}\text{Sn}_{0.94}\text{Se}_2\text{S}$  into a highly degenerate



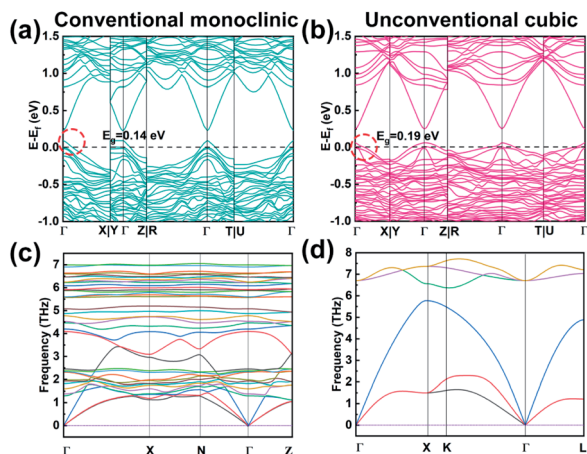


Fig. 3 The electronic energy band structures for (a) monoclinic  $\text{Cu}_{1.87}\text{Ag}_{0.13}(\text{In}_{0.06}\text{Sn}_{0.94})\text{Se}_2\text{S}$  and (b) cubic  $\text{Cu}_{1.87}\text{Ag}_{0.13}(\text{In}_{0.06}\text{Sn}_{0.94})\text{Se}_2\text{S}$ . The phonon dispersions of (c) monoclinic  $\text{Cu}_2\text{SnSe}_3$  and (d) cubic  $\text{Cu}_2\text{SnSe}_3$ .

semiconductor (Fig. S15e and f<sup>†</sup>), which thus increases channels for electrical transport. From the valence bands near the Fermi level that are highlighted by the red circles in Fig. 3a and b and S15,† we find that the top three valence bands at the  $\Gamma$  point of the monoclinic structure display band splitting while the cubic structure is degenerate. The cubic phase with high degeneracy can lead to more energy valleys participating in electrical transport.<sup>13</sup>

To gain insight into phonon and thermal properties, we calculated the phonon dispersion relations of monoclinic and cubic  $\text{Cu}_2\text{SnSe}_3$  based on DFT, as shown in Fig. 3c and d. The monoclinic phase has 12 atoms in a primitive cell and thus 36 phonon branches (Fig. S16a<sup>†</sup>). The cubic phase has a zinc blende structure, in which Cu and Sn randomly occupy the cation sites with a ratio of 2 : 1, and Se occupies the anion sites (Fig. S16b<sup>†</sup>). We used the virtual crystal approximation (VCA) to calculate the phonon dispersion of the cubic phase. Under VCA, the cubic phase has a primitive cell that consists of 2 atoms – a virtual atom, made of 2/3 Cu and 1/3 Sn, and a Se atom. The phonon dispersion of the cubic phase does not show any imaginary frequency, indicating that the structure is locally stable. The maximum frequency of the cubic phase is larger than that of the monoclinic phase, indicating that the cubic phase may have stronger bonds. The phonon group velocity, especially for the longitudinal acoustic (LA) branch, of the cubic phase is much larger than that of the monoclinic phase (Fig. S16c<sup>†</sup>). The volumetric heat capacity of the cubic phase is slightly larger than that of the monoclinic phase (Fig. S16d<sup>†</sup>), partially because the cubic phase has higher symmetry and packing density. Based on phonon kinetic theory, the lattice thermal conductivity is  $k_L = 1/3cv^2\tau$ , in which  $c$  is the heat capacity,  $v$  is the group velocity, and  $\tau$  is the phonon relaxation time. Since the cubic phase has larger  $c$  and  $v$  than the monoclinic phase, its  $\tau$  must be much smaller, in order to have similar or lower  $k_L$ . This inference indicates that the disorder and distortion induced by Cu/Sn alloying that was not considered in the VCA in the cubic phase must be strong and induce

severe phonon scattering. Additionally, grain boundaries, dislocations, Ag and S alloying and In doping further reduce the phonon relaxation time.

## 2.4 Thermoelectric properties

**2.4.1. Sulfur alloying at the anionic site.** Fig. S19<sup>†</sup> shows the thermoelectric properties of  $\text{Cu}_2\text{SnSe}_3$  and  $\text{Cu}_2\text{SnSe}_2\text{S}$  in the temperature range of 323–873 K. It is found that S-alloying leads to a clear decrease in electrical conductivity ( $\sigma$ ) (Fig. S19a<sup>†</sup>). The positive Seebeck coefficient ( $S$ ) (Fig. S19b<sup>†</sup>) indicates that the major charge carrier is holes. The  $S$  values of  $\text{Cu}_2\text{SnSe}_3$  and  $\text{Cu}_2\text{SnSe}_2\text{S}$  increase with rising temperature. Specifically,  $S$  increases from 28.15  $\mu\text{V K}^{-1}$  for  $\text{Cu}_2\text{SnSe}_3$  to 133.62  $\mu\text{V K}^{-1}$  for  $\text{Cu}_2\text{SnSe}_2\text{S}$  at 323 K by partial replacement of Se with S. Despite the enhanced Seebeck coefficient, the power factor (PF) of  $\text{Cu}_2\text{SnSe}_2\text{S}$  (0.37  $\text{mW m}^{-1} \text{K}^{-2}$  at 873 K) is smaller than that of  $\text{Cu}_2\text{SnSe}_3$  (0.58  $\text{mW m}^{-1} \text{K}^{-2}$  at 873 K) (Fig. S19c<sup>†</sup>) because of the lower electrical conductivity.  $\text{Cu}_2\text{SnSe}_2\text{S}$  has a low thermal conductivity ( $k_{\text{tot}}$ ) of 0.43  $\text{W m}^{-1} \text{K}^{-1}$ , which is about 47% lower than that of non-alloyed  $\text{Cu}_2\text{SnSe}_3$  (Fig. S19d<sup>†</sup>), indicating the role of S alloying in reducing  $k$ . This result may be caused by the distortion and diminished uniformity of the lattice structure, as well as the coexistence of the minor secondary phase of  $\text{Cu}_{1.8}\text{Se}$ , which enhances the scattering of phonons. Since the large decrease in  $k_{\text{tot}}$  overwhelms the decreased PF, the  $ZT$  value of the  $\text{Cu}_2\text{SnSe}_2\text{S}$  nanostructured solid is 0.75 at 873 K, higher than that of  $\text{Cu}_2\text{SnSe}_3$  (Fig. S19e<sup>†</sup>).

**2.4.2. Ag and In alloying at the cationic site.** Fig. 4a depicts the temperature dependence of  $\sigma$  of  $\text{Cu}_{2-y}\text{Ag}_y(\text{In}_x\text{Sn}_{1-x})\text{Se}_2\text{S}$  ( $x = 0, 0.05, 0.06, 0.25, y = 0, 0.07, 0.13$ ), which show complex dependence on the  $x$  and  $y$  values. Ag alloying can increase  $\sigma$  from  $7.06 \times 10^3 \text{ S m}^{-1}$  for  $\text{Cu}_2\text{In}_{0.06}\text{Sn}_{0.94}\text{Se}_2\text{S}$  to  $9.18 \times 10^3 \text{ S m}^{-1}$  for  $\text{Cu}_{1.93}\text{Ag}_{0.07}(\text{In}_{0.06}\text{Sn}_{0.94})\text{Se}_2\text{S}$  at 873 K. Fig. 4b shows  $S$  of  $\text{Cu}_{2-y}\text{Ag}_y(\text{In}_x\text{Sn}_{1-x})\text{Se}_2\text{S}$  for different values of  $x$  and  $y$ .  $S$  increases with increasing temperature in the range of 323–723 K and then decreases slightly in the high-temperature zone, which may be ascribed to the thermal excitation of minority carriers. Moreover, with an increase in the amount of In,  $S$  is boosted from 197  $\mu\text{V K}^{-1}$  for  $\text{Cu}_2\text{SnSe}_2\text{S}$  to 298  $\mu\text{V K}^{-1}$  for  $\text{Cu}_2\text{In}_{0.25}\text{Sn}_{0.75}\text{Se}_2\text{S}$  at 873 K. Fig. 4d shows the  $k_{\text{tot}}$  of  $\text{Cu}_{2-y}\text{Ag}_y(\text{In}_x\text{Sn}_{1-x})\text{Se}_2\text{S}$ . A significant reduction in  $k_{\text{tot}}$  upon doping In at the Sn site and/or alloying Ag at the Cu site is found, demonstrating the important role of entropy effects.

**2.4.3. High crystallographic symmetry leads to high Seebeck coefficient and power factor.** In order to understand the electrical transport, effective mass analysis by the Pisarenko plot was done, as shown in Fig. 5a. Compared with the largest  $m_d^* = 3.1m_e$  ( $m_e$  is the free electron mass) in the monoclinic-phase  $\text{Cu}_2\text{Sn}_{1-y}\text{In}_y\text{Se}_{2.7}\text{S}_{0.3}$  and  $\text{Cu}_{2-x}\text{Ag}_x\text{Sn}_{1-y}\text{In}_y\text{Se}_3$  reported by Ming *et al.*<sup>35</sup> and Li *et al.*,<sup>34</sup> the enhancement in symmetry increases the effective mass to  $4.0m_e$  in our cubic  $\text{Cu}_2\text{In}_{0.06}\text{Sn}_{0.94}\text{Se}_2\text{S}$  sample, yielding a large Seebeck coefficient. As shown in Fig. 4c, the PF further increases *via* Ag alloying in the whole investigated temperature range. The maximum PF values of 0.45 and 0.44  $\text{mW m}^{-1} \text{K}^{-2}$  are obtained at 873 K for



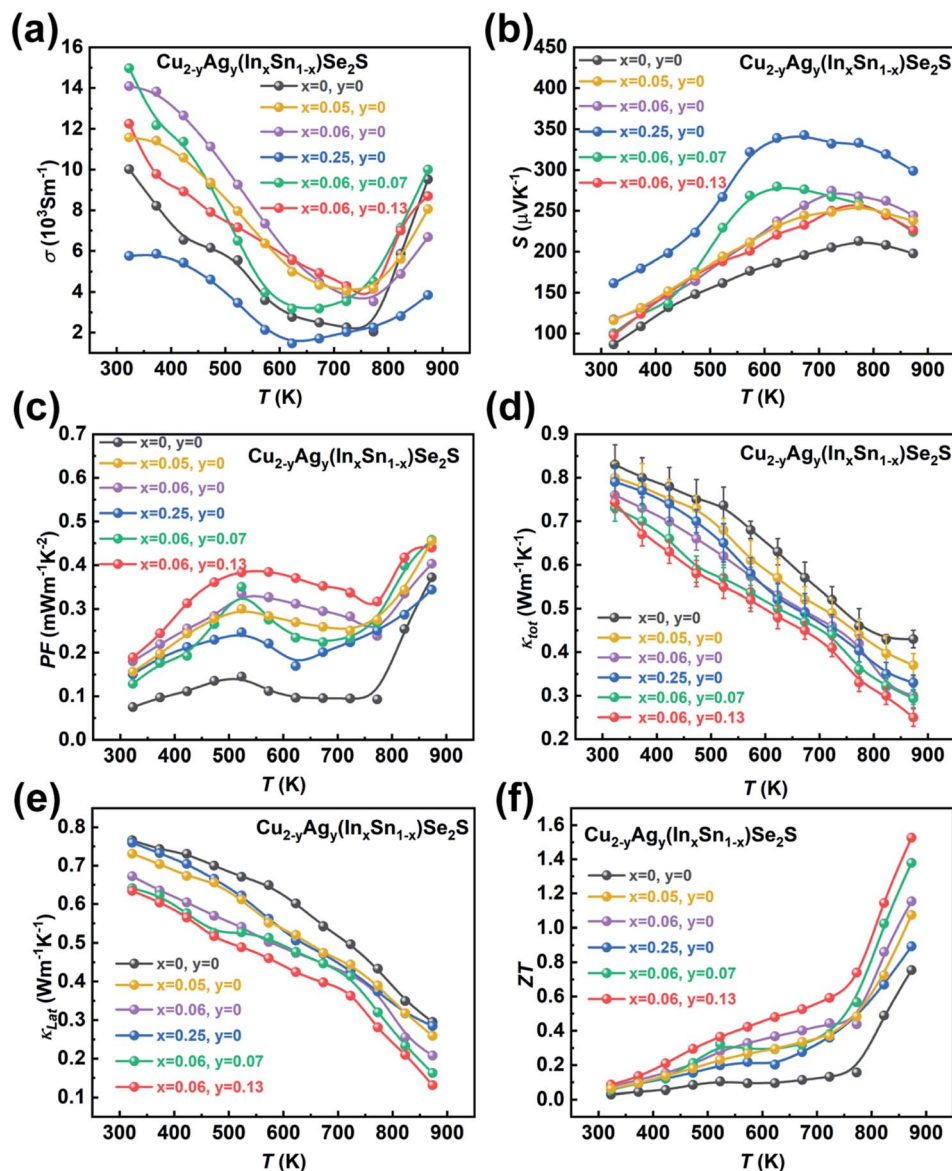


Fig. 4 Temperature dependence of (a) electrical conductivity  $\sigma$ , (b) Seebeck coefficient  $S$ , (c) power factor  $PF$ , (d) total thermal conductivity  $k_{\text{tot}}$ , (e) lattice thermal conductivity  $k_{\text{lat}}$  and (f)  $ZT$  values for  $\text{Cu}_{2-y}\text{Ag}_y(\text{In}_x\text{Sn}_{1-x})\text{Se}_2\text{S}$  ( $x = 0, 0.05, 0.06, 0.25, y = 0, 0.07, 0.13$ ).

$\text{Cu}_{1.93}\text{Ag}_{0.07}(\text{In}_{0.06}\text{Sn}_{0.94})\text{Se}_2\text{S}$  and  $\text{Cu}_{1.87}\text{Ag}_{0.13}(\text{In}_{0.06}\text{Sn}_{0.94})\text{Se}_2\text{S}$ , respectively.

**2.4.4. Unique crystal structure and nanostructures lead to ultralow thermal conductivity.** The temperature-dependent total ( $k_{\text{tot}}$ ) and lattice ( $k_{\text{lat}}$ ) thermal conductivity for all the samples decline with increasing temperature in the whole investigated temperature range, as exhibited in Fig. 4d and e. The  $k_{\text{lat}}$  is calculated by  $k_{\text{lat}} = k_{\text{tot}} - k_{\text{e}}$ , in which  $k_{\text{e}}$  is electronic thermal conductivity and is estimated using the Wiedemann-Franz law, *i.e.*,  $k_{\text{e}} = L\sigma T$ , where  $L$  is the Lorentz factor, calculated based on the single parabolic band (SPB) assumption. The  $k_{\text{tot}}$  and  $k_{\text{lat}}$  gradually decrease with In doping, but increase with more In content doping, which should be attributed to the reduction of secondary phase and the decrease of atomic disorder resulting from the transition to the tetragonal phase.

Furthermore, the substitution of Ag on the Cu site further decreases the  $k_{\text{tot}}$  and  $k_{\text{lat}}$  down to 0.25 and 0.13  $\text{W m}^{-1} \text{K}^{-1}$  respectively at 873 K for the  $\text{Cu}_{1.87}\text{Ag}_{0.13}(\text{In}_{0.06}\text{Sn}_{0.94})\text{Se}_2\text{S}$  sample due to the enhanced scattering of phonons resulting from the distortion and diminished uniformity of the lattice structure, which is comparable to some reported materials with extremely low  $k$ , such as  $\text{AgSbTe}_2$ ,<sup>55</sup>  $\text{Bi}_4\text{O}_4\text{SeCl}_2$  (ref. 56) and  $\text{TlCuSe}$ .<sup>57</sup> Compared to the thermal conductivity reported in  $\text{Cu}_2\text{SnSe}_3$ -based systems in the literature,<sup>34–36,39</sup> our value is relatively low, as shown in Fig. 5c.

The ultralow  $k_{\text{lat}}$  of the as-synthesized samples can be attributed to the following three reasons. First, the intrinsic crystal structure of  $\text{Cu}_2\text{SnSe}_3$ -based materials leads to low phonon thermal conductivity. More specifically, the Cu–Se bond constructs a conductive framework for controlling hole



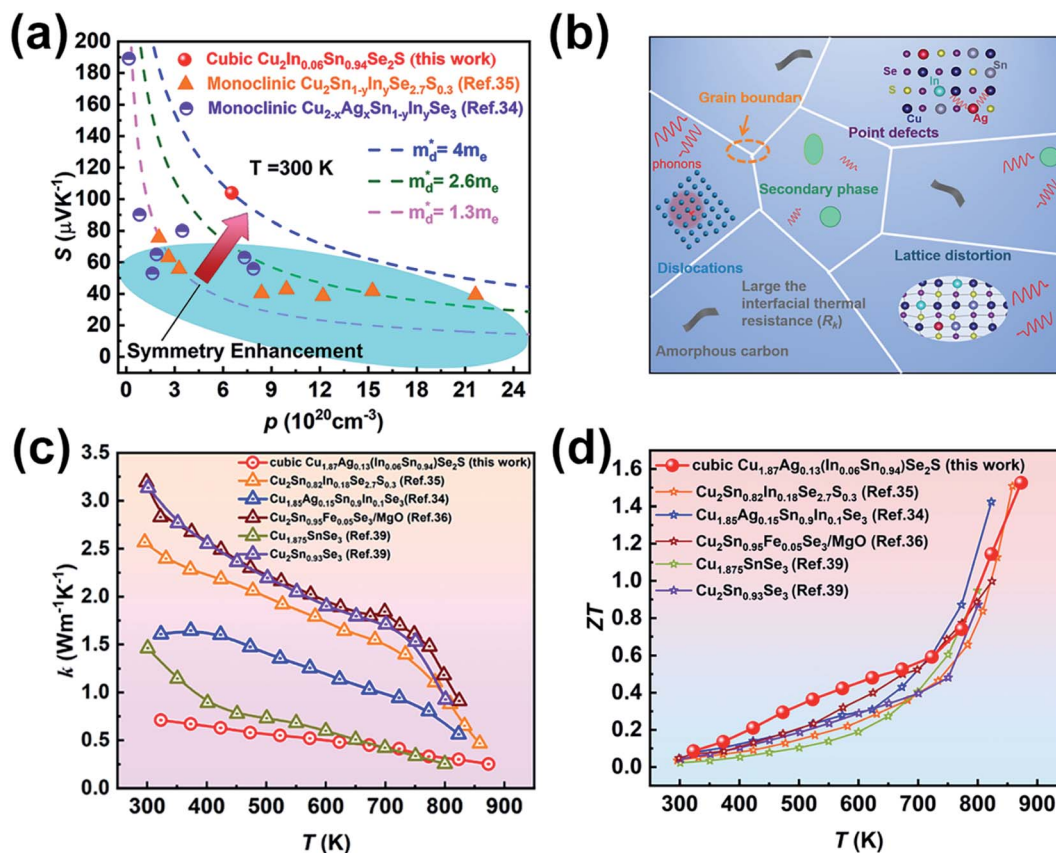


Fig. 5 (a) Variation of Seebeck coefficient  $S$  with carrier concentration  $p$  for cubic  $\text{Cu}_2\text{In}_{0.06}\text{Sn}_{0.94}\text{Se}_2\text{S}$ , in which the blue dotted line is the Pisarenko curve obtained via the SPB model. The previously reported data by Ming *et al.*<sup>35</sup> (monoclinic  $\text{Cu}_2\text{Sn}_{1-y}\text{In}_y\text{Se}_{2.7}\text{S}_{0.3}$ ,  $y = 0-0.21$ ) and Li *et al.*<sup>34</sup> (monoclinic  $\text{Cu}_{2-x}\text{Ag}_x\text{Sn}_{1-y}\text{In}_y\text{Se}_3$ ,  $x = 0-0.15$ ,  $y = 0-0.15$ ) are depicted by orange triangles and purple half-filled circles, respectively. (b) Schematic illustration of the effect of multiscale defects on phonons, including grain boundaries, point defects, lattice distortion, secondary phase, dislocations and amorphous carbon. Comparison of the reported (c) thermal conductivity and (d)  $ZT$  values of  $\text{Cu}_2\text{SnSe}_3$ -based materials.<sup>34-36,39</sup>

transport, and cationic doping is allowed to adjust the carrier concentration.<sup>58</sup> Such structural characteristics are similar to those of phonon glass electron crystal (PGEC) compounds,<sup>50,51</sup> which can be confirmed by low-temperature  $C_p$  measurement (Fig. S22†). The plot of  $C_p$  vs.  $T$  can be fitted by a Debye model combined with three Einstein modes (black line, the detailed calculation is shown in the ESI†), which illustrates that the contribution to  $C_p$  at low temperature is dominated by low-energy optical modes resulting from the weakly bound Cu or Ag-rattlers (Einstein oscillators) that suppress lattice thermal conductivity ( $k_{\text{lat}}$ ).<sup>59-61</sup> Second, the configurational entropy in a material increases through doping and alloying (Fig. S23†). Based on the Boltzmann hypothesis, the configurational entropy ( $\Delta S$ ) is given by:<sup>27</sup>

$$\Delta S = k_B \ln \Omega = -N_A k_B \sum_{i=1}^n x_i \ln x_i \quad (1)$$

where  $k_B$  is the Boltzmann constant,  $\Omega$  is the atomic occupation probability,  $n$  is the number of substituted components,  $x_i$  is the mole content of the  $i$ th component, and  $N_A$  is Avogadro's number. Among the various components, the possibility of each element having the same lattice size and different atomic size

and electronegativity results in lattice distortion,<sup>62</sup> which can be confirmed by the PDF result in Fig. 1e. Short-range disordered structure of multi-component high-entropy materials caused by severe lattice distortion can strongly scatter heat-carrying phonons, reducing the material's lattice thermal conductivity down to its theoretical minimum value. Third, the nano-sized grain effects (boundary scattering) and multidimensional defects (*i.e.*, minor secondary phase of  $\text{Cu}_{1.8}\text{Se}$ , point defects, dislocations, and strain fields) (Fig. 5b) induce severe phonon scattering and efficiently reduce the lattice thermal conductivity. Additionally, the amorphous carbon formed by carbonization of ligands after SPS could result in the reduction of thermal conductivity  $k$  due to the large interfacial thermal resistance ( $R_k$ ) resulting from the high dissimilarity in density, sound velocity, and phonon density of states between carbon and the semiconductor matrix.<sup>63,64</sup>

Fig. 4f shows the temperature dependence of  $ZT$  values for  $\text{Cu}_{2-y}\text{Ag}_y(\text{In}_x\text{Sn}_{1-x})\text{Se}_2\text{S}$ . Owing to the high PF and low thermal conductivity,  $\text{Cu}_{1.87}\text{Ag}_{0.13}(\text{In}_{0.06}\text{Sn}_{0.94})\text{Se}_2\text{S}$  shows the maximum  $ZT$  of 1.52 at 873 K. Compared to the  $ZT$  values reported in  $\text{Cu}_2\text{SnSe}_3$ -based systems in the literature,<sup>34-36,39</sup> our value is essentially record-high, as shown in Fig. 5d. Compared with the



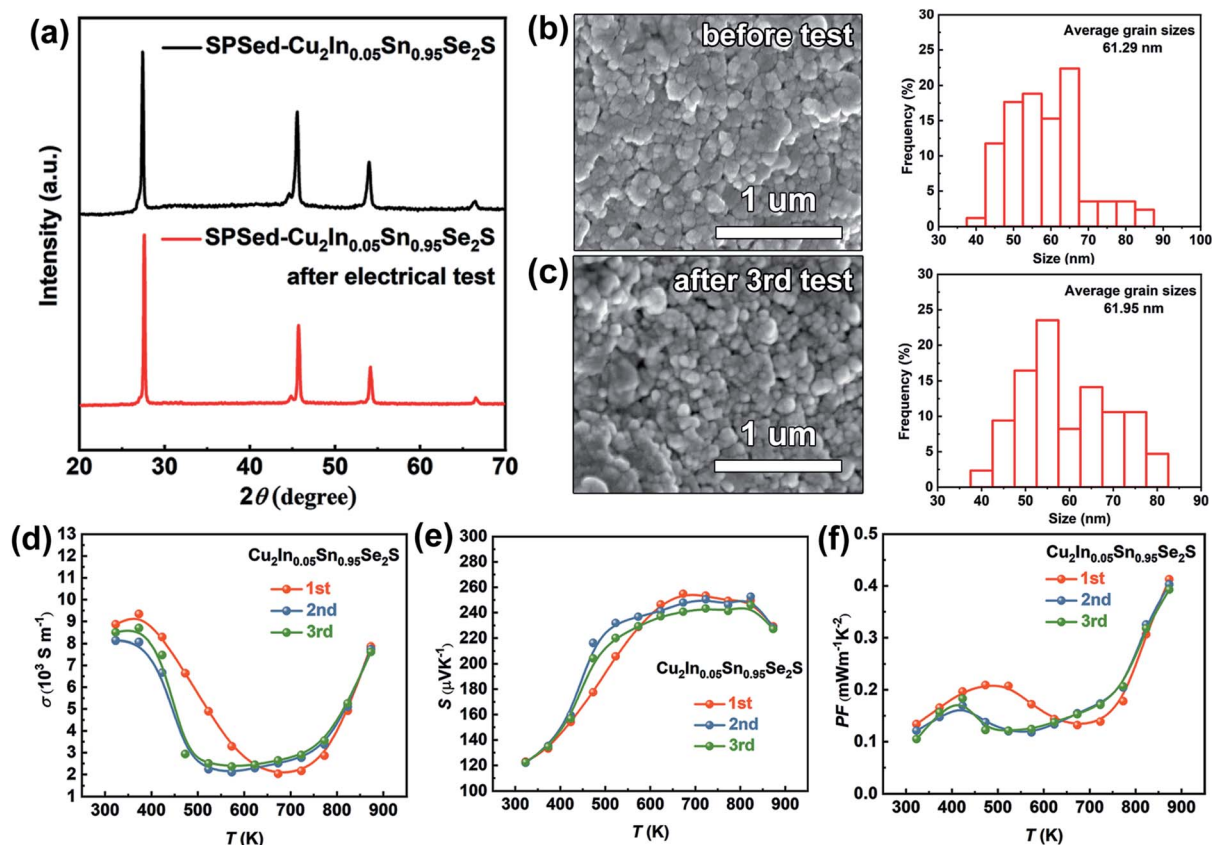


Fig. 6 The thermal stability tests for  $\text{Cu}_2\text{In}_{0.05}\text{Sn}_{0.95}\text{Se}_2\text{S}$ . (a) XRD patterns before testing and after the 3rd electrical test. (b and c) SEM micrographs of sintered pellets before testing and after three rounds of electrical tests. (d–f) Cyclic tests of electrical conductivity  $\sigma$ , Seebeck coefficient  $S$  and power factor  $PF$ .

$k_{\text{lat}}$  and carrier mobility ( $\mu_{\text{H}}$ ) at  $\sim 300$  K in the monoclinic-phase  $\text{Cu}_2\text{Sn}_{0.82}\text{In}_{0.18}\text{Se}_{2.7}\text{S}_{0.3}$  and  $\text{Cu}_{1.85}\text{Ag}_{0.15}\text{Sn}_{0.9}\text{In}_{0.1}\text{Se}_3$  reported by Ming *et al.*<sup>35</sup> and Li *et al.*,<sup>34</sup> a relatively low  $k_{\text{lat}}$  and  $\mu_{\text{H}}$  (Table S5<sup>†</sup>) are obtained in our cubic  $\text{Cu}_2\text{In}_{0.06}\text{Sn}_{0.94}\text{Se}_2\text{S}$  sample due to the nano-grain size, which enhances the grain boundary scattering for the charge carrier. The ultralow  $k_{\text{lat}}$  can compensate for the deterioration in electrical conductivity, which can be understood from the quality factor,<sup>65</sup>  $\beta = (\mu_{\text{H}}/k_{\text{lat}})(m_{\text{d}}^*/m_{\text{e}})^{3/2}$  (Table S5<sup>†</sup>), taking into account the  $k_{\text{lat}}$  and  $\mu_{\text{H}}$  in the numerator and denominator, respectively.

The reproducibility of thermoelectric performance for  $\text{Cu}_{1.87}\text{Ag}_{0.13}(\text{In}_{0.06}\text{Sn}_{0.94})\text{Se}_2\text{S}$  is provided in Fig. S24.<sup>†</sup> Besides, the thermal stability is a critical concern for metastable phases in the thermoelectric community. Thus, the XRD patterns of SPSed- $\text{Cu}_2\text{In}_{0.05}\text{Sn}_{0.95}\text{Se}_2\text{S}$  before testing and after the 3rd electrical test were measured, and no change in phase structure is found (Fig. 6a). Additionally, after measuring the electrical properties three times, the SPSed- $\text{Cu}_2\text{In}_{0.05}\text{Sn}_{0.95}\text{Se}_2\text{S}$  sample could still maintain the same grain size (Fig. 6b and c). The electrical performance was re-measured three times for  $\text{Cu}_2\text{In}_{0.05}\text{Sn}_{0.95}\text{Se}_2\text{S}$  and shows no deterioration (Fig. 6d–f).

### 3. Conclusions

In summary, we have successfully synthesized a high-entropy system,  $\text{Cu}_{2-y}\text{Ag}_y(\text{In}_x\text{Sn}_{1-x})\text{Se}_2\text{S}$  ( $x = 0-0.25$ ,  $y = 0, 0.07, 0.13$ ),

by adopting a hot-injection strategy and characterized the thermoelectric properties of dense materials compacted from those nanoparticles. We propose a new synthetic route for compacting nanocrystals without eliminating long organic ligands and subsequently obtain a series of high-entropy multinary chalcogenide nanocrystals with a metastable cubic phase induced by size-driven structural stabilization. Through phase and entropy design, a high power factor ( $0.44 \text{ mW m}^{-1} \text{ K}^{-2}$ ) and an ultralow thermal conductivity ( $0.25 \text{ W m}^{-1} \text{ K}^{-1}$ ) are achieved at 873 K for the  $\text{Cu}_{1.87}\text{Ag}_{0.13}(\text{In}_{0.06}\text{Sn}_{0.94})\text{Se}_2\text{S}$  sample. A high  $ZT$  of 1.52 is achieved which is about 204% higher than that of pristine  $\text{Cu}_2\text{SnSe}_3$ . This work provides a new strategy for stabilizing the metastable phase through ligand retention induced small size and may have broader application in various fields such as photocatalysis, electronic devices, and photovoltaics.

### Data availability

Chemicals, preparation of  $\text{Cu}_2\text{SnSe}_3$ ,  $\text{Cu}_2\text{SnSe}_2\text{S}$ ,  $\text{Cu}_2\text{In}_x\text{Sn}_{1-x}\text{Se}_2\text{S}$ ,  $\text{Cu}_3\text{InSnSe}_3\text{S}_2$  and  $\text{Cu}_{2-y}\text{Ag}_y(\text{In}_{0.06}\text{Sn}_{0.94})\text{Se}_2\text{S}$  nanocrystals, spark plasma sintering, characterization, measurement of thermoelectric properties, DFT calculation, formation energy calculation, the calculation details of Lorentz factor ( $L$ ) and density of states effective mass ( $m_{\text{d}}^*$ ) via single parabolic band (SPB) model, the calculation details of heat capacity  $C_{\text{p}}$  via the Debye-3 Einstein model, crystal structure characterization,



microstructure and composition, electronic and phononic band structures and thermoelectric properties are available in the ESI.†

## Author contributions

Wanjia Zhang: investigation, methodology, data curation, formal analysis, visualization, writing – original draft. Yue Lou: resources, supervision, writing – review & editing. Hongliang Dong: synchrotron X-ray diffraction testing. Fanshi Wu: formal analysis, DFT calculation, writing – original draft. Janak Tiwari: formal analysis, DFT calculation, writing – original draft. Zhan Shi: resources, writing – reviewing. Sokrates T. Pantelides: supervision, writing – reviewing. Tianli Feng: conceptualization, DFT calculation, writing – review & editing, supervision. Biao Xu: conceptualization, writing – review & editing, supervision, project administration, funding acquisition.

## Conflicts of interest

The authors declare no competing financial interest.

## Acknowledgements

B. X. is thankful for financial support from Jiangsu Specially Appointed Professorship, the Jiangsu Provincial Innovation and Entrepreneurship Doctor Program, and the 1000 Young Talents Program. Y. L. is thankful for financial support from the Jiangsu Provincial Innovation and Entrepreneurship Doctor Program (JSSCBS20210215). The support and resources from the Center for High-Performance Computing at the University of Utah and the National Energy Research Scientific Computing Center (NERSC) are gratefully acknowledged. We thank the staff of the BL17B1 beamline of the National Facility for Protein Science in Shanghai (NFPS) at the Shanghai Synchrotron Radiation Facility.

## References

- B. Hu, X.-L. Shi, J. Zou and Z.-G. Chen, *Chem. Eng. J.*, 2022, **437**, 135268.
- L. Li, W. D. Liu, Q. Liu and Z. G. Chen, *Adv. Funct. Mater.*, 2022, **32**, 2200548.
- Z.-G. Chen and W.-D. Liu, *J. Mater. Sci. Technol.*, 2022, **121**, 256–262.
- W.-Y. Chen, X.-L. Shi, J. Zou and Z.-G. Chen, *Small Methods*, 2022, **6**, 2101235.
- M. Li, M. Hong, M. Dargusch, J. Zou and Z.-G. Chen, *Trends Chem.*, 2021, **3**, 561–574.
- Z.-Z. Luo, S. Cai, S. Hao, T. P. Bailey, I. Spanopoulos, Y. Luo, J. Xu, C. Uher, C. Wolverton, V. P. Dravid, Q. Yan and M. G. Kanatzidis, *Angew. Chem., Int. Ed.*, 2021, **60**, 268–273.
- Q. Liu, Z. Zhao, Y. Lin, P. Guo, S. Li, D. Pan and X. Ji, *Chem. Commun.*, 2011, **47**, 964–966.
- D. Sarkar, T. Ghosh, A. Banik, S. Roychowdhury, D. Sanyal and K. Biswas, *Angew. Chem., Int. Ed.*, 2020, **59**, 11115–11122.
- Y. Pei, X. Shi, A. LaLonde, H. Wang, L. Chen and G. J. Snyder, *Nature*, 2011, **473**, 66–69.
- J. P. Heremans, B. Wiendlocha and A. M. Chamoire, *Energy Environ. Sci.*, 2012, **5**, 5510–5530.
- J. P. Heremans, V. Jovovic, E. S. Toberer, A. Saramat, K. Kurosaki, A. Charoenphakdee, S. Yamanaka and G. J. Snyder, *Science*, 2008, **321**, 554–557.
- L. Hu, T. Zhu, X. Liu and X. Zhao, *Adv. Funct. Mater.*, 2014, **24**, 5211–5218.
- L. Hu, Y. Luo, Y.-W. Fang, F. Qin, X. Cao, H. Xie, J. Liu, J. Dong, A. Sanson, M. Giarola, X. Tan, Y. Zheng, A. Suwardi, Y. Huang, K. Hippalgaonkar, J. He, W. Zhang, J. Xu, Q. Yan and M. G. Kanatzidis, *Adv. Energy Mater.*, 2021, **11**, 2100661.
- Y. Kinemuchi, M. Mikami, K. Kobayashi, K. Watari and Y. Hotta, *J. Electron. Mater.*, 2010, **39**, 2059–2063.
- K. Peng, H. Wu, Y. Yan, L. Guo, G. Wang, X. Lu and X. Zhou, *J. Mater. Chem. A*, 2017, **5**, 14053–14060.
- X.-L. Shi, W.-D. Liu, M. Li, Q. Sun, S.-D. Xu, D. Du, J. Zou and Z.-G. Chen, *Adv. Energy Mater.*, 2022, **12**, 2200670.
- M. Li, Q. Sun, S.-D. Xu, M. Hong, W.-Y. Lyu, J.-X. Liu, Y. Wang, M. Dargusch, J. Zou and Z.-G. Chen, *Adv. Mater.*, 2021, **33**, 2102575.
- W.-D. Liu, Y. Yu, M. Dargusch, Q. Liu and Z.-G. Chen, *Renewable Sustainable Energy Rev.*, 2021, **141**, 110800.
- W.-D. Liu, L. Yang and Z.-G. Chen, *Nano Today*, 2020, **35**, 100938.
- Y. Sun, C.-A. Di, W. Xu and D. Zhu, *Adv. Electron. Mater.*, 2019, **5**, 1800825.
- B. Bai, M. Xu, N. Li, W. Chen, J. Liu, J. Liu, H. Rong, D. Fenske and J. Zhang, *Angew. Chem., Int. Ed.*, 2019, **58**, 4852–4857.
- H. F. Cheng, N. L. Yang, Q. P. Lu, Z. C. Zhang and H. Zhang, *Adv. Mater.*, 2018, **30**, 1707189.
- J. Liu, J. Huang, W. Niu, C. Tan and H. Zhang, *Chem. Rev.*, 2021, **121**, 5830–5888.
- Y. Chen, Z. Lai, X. Zhang, Z. Fan, Q. He, C. Tan and H. Zhang, *Nat. Rev. Chem.*, 2020, **4**, 243–256.
- Y. Luo, T. Xu, Z. Ma, D. Zhang, Z. Guo, Q. Jiang, J. Yang, Q. Yan and M. G. Kanatzidis, *J. Am. Chem. Soc.*, 2021, **143**, 13990–13998.
- S. Roychowdhury, T. Ghosh, R. Arora, U. V. Waghmare and K. Biswas, *Angew. Chem., Int. Ed.*, 2018, **57**, 15167–15171.
- H. Zhu, T. Zhao, B. Zhang, Z. An, S. Mao, G. Wang, X. Han, X. Lu, J. Zhang and X. Zhou, *Adv. Energy Mater.*, 2021, **11**, 2003304.
- L. Hu, Y. Zhang, H. Wu, J. Li, Y. Li, M. McKenna, J. He, F. Liu, S. J. Pennycook and X. Zeng, *Adv. Energy Mater.*, 2018, **8**, 1802116.
- B. Jiang, Y. Yu, J. Cui, X. Liu, L. Xie, J. Liao, Q. Zhang, Y. Huang, S. Ning, B. Jia, B. Zhu, S. Bai, L. Chen, S. J. Pennycook and J. He, *Science*, 2021, **371**, 830–834.
- Y. Luo, S. Hao, S. Cai, T. J. Slade, Z. Z. Luo, V. P. Dravid, C. Wolverton, Q. Yan and M. G. Kanatzidis, *J. Am. Chem. Soc.*, 2020, **142**, 15187–15198.
- H. Duan, Z. Cheng, Y. Xue, Z. Cui, M. Yang and S. Wang, *J. Electroanal. Chem.*, 2021, **882**, 115037.



- 32 M. Wang, Z. Cui, Y. Xue, A. Yan, X. Yu, X. Song and H. Li, *Electroanalysis*, 2019, **31**, 1316–1323.
- 33 C. Wang, Z. Cui, Y. Xue, Y. Wang, M. Wang, B. Ji, J. Chen, Y. Xue and L. Zhang, *Thermochim. Acta*, 2022, **708**, 179140.
- 34 Y. Li, G. Liu, T. Cao, L. Liu, J. Li, K. Chen, L. Li, Y. Han and M. Zhou, *Adv. Funct. Mater.*, 2016, **26**, 6025–6032.
- 35 H. Ming, G. Zhu, C. Zhu, X. Qin, T. Chen, J. Zhang, D. Li, H. Xin and B. Jabar, *ACS Nano*, 2021, **15**, 10532–10541.
- 36 H. Ming, C. Zhu, X. Qin, J. Zhang, D. Li, B. Zhang, T. Chen, J. Li, X. Lou and H. Xin, *ACS Appl. Mater. Interfaces*, 2020, **12**, 19693–19700.
- 37 E. J. Skoug, J. D. Cain and D. T. Morelli, *J. Alloys Compd.*, 2010, **506**, 18–21.
- 38 R. Ma, G. Liu, Y. Li, J. Li, K. Chen, Y. Han, M. Zhou and L. Li, *J. Asian Ceram. Soc.*, 2018, **6**, 13–19.
- 39 X. Cheng, Z. Li, Y. You, T. Zhu, Y. Yan, X. Su and X. Tang, *ACS Appl. Mater. Interfaces*, 2019, **11**, 24212–24220.
- 40 Y. Zhou, H. Wu, D. Wang, L. Fu, Y. Zhang, J. He, S. J. Pennycook and L. D. Zhao, *Mater. Today Phys.*, 2018, **7**, 77–88.
- 41 G. Marcano, C. Rincón, S. A. López, G. Sánchez Pérez, J. L. Herrera-Pérez, J. G. Mendoza-Alvarez and P. Rodríguez, *Solid State Commun.*, 2011, **151**, 84–86.
- 42 H. Ming, C. Zhu, X. Qin, B. Jabar, T. Chen, J. Zhang, H. Xin, D. Li and J. Zhang, *Nanoscale*, 2021, **13**, 4233–4240.
- 43 Y. Lou, W. Zhao, C. Li, H. Huang, T. Bai, C. Chen, C. Liang, Z. Shi, D. Zhang, X.-B. Chen and S. Feng, *ACS Appl. Mater. Interfaces*, 2017, **9**, 18046–18053.
- 44 Y. Liu, M. Calcabrini, Y. Yu, S. Lee, C. Chang, J. David, T. Ghosh, M. C. Spadaro, C. Xie, O. Cojocaru-Mirédin, J. Arbiol and M. Ibáñez, *ACS Nano*, 2022, **16**, 78–88.
- 45 F.-J. Fan, L. Wu and S.-H. Yu, *Energy Environ. Sci.*, 2014, **7**, 190–208.
- 46 X. Wang, X. Liu, D. Yin, Y. Ke and M. T. Swihart, *Chem. Mater.*, 2015, **27**, 3378–3388.
- 47 W. W. Yu, Y. A. Wang and X. Peng, *Chem. Mater.*, 2003, **15**, 4300–4308.
- 48 M. E. Norako, M. J. Greaney and R. L. Brutchey, *J. Am. Chem. Soc.*, 2012, **134**, 23–26.
- 49 J. Jeong, H. Chung, Y. C. Ju, J. Moon, J. Roh, S. Yoon, Y. R. Do and W. Kim, *Mater. Lett.*, 2010, **64**, 2043–2045.
- 50 M. Beekman, D. T. Morelli and G. S. Nolas, *Nat. Mater.*, 2015, **14**, 1182–1185.
- 51 *CRC Handbook of Thermoelectrics*, ed. G. A. Slack and D. M. Rowe, CRC Press, Boca Raton, FL, USA, 1995.
- 52 M. B. Sigman, A. Ghezelbash, T. Hanrath, A. E. Saunders, F. Lee and B. A. Korgel, *J. Am. Chem. Soc.*, 2003, **125**, 16050–16057.
- 53 W. P. Lim, C. T. Wong, S. L. Ang, H. Y. Low and W. S. Chin, *Chem. Mater.*, 2006, **18**, 6170–6177.
- 54 Y. Yu, C. Zhou, S. Zhang, M. Zhu, M. Wuttig, C. Scheu, D. Raabe, G. J. Snyder, B. Gault and O. Cojocaru-Mirédin, *Mater. Today*, 2020, **32**, 260–274.
- 55 S. Roychowdhury, T. Ghosh, R. Arora, M. Samanta, L. Xie, N. K. Singh, A. Soni, J. He, U. V. Waghmare and K. Biswas, *Science*, 2021, **371**, 722–727.
- 56 Q. D. Gibson, T. Zhao, L. M. Daniels, H. C. Walker, R. Daou, S. Hébert, M. Zanella, M. S. Dyer, J. B. Claridge, B. Slater, M. W. Gaultois, F. Corà, J. Alaria and M. J. Rosseinsky, *Science*, 2021, **373**, 1017–1022.
- 57 W. Lin, J. He, X. Su, X. Zhang, Y. Xia, T. P. Bailey, C. C. Stoumpos, G. Tan, A. J. E. Rettie, D. Y. Chung, V. P. Dravid, C. Uher, C. Wolverton and M. G. Kanatzidis, *Adv. Mater.*, 2021, **33**, 2104908.
- 58 X. Shi, L. Xi, J. Fan, W. Zhang and L. Chen, *Chem. Mater.*, 2010, **22**, 6029–6031.
- 59 M. K. Jana, K. Pal, A. Warankar, P. Mandal, U. V. Waghmare and K. Biswas, *J. Am. Chem. Soc.*, 2017, **139**, 4350–4353.
- 60 J. L. Baker, J. T. White, A. Chen, T. Ulrich, R. R. Roback and H. Xu, *J. Nucl. Mater.*, 2021, **557**, 153282.
- 61 B. Koley, A. Lakshan, P. R. Raghuvanshi, C. Singh, A. Bhattacharya and P. P. Jana, *Angew. Chem., Int. Ed.*, 2021, **60**, 9106–9113.
- 62 R. Liu, H. Chen, K. Zhao, Y. Qin, B. Jiang, T. Zhang, G. Sha, X. Shi, C. Uher, W. Zhang and L. Chen, *Adv. Mater.*, 2017, **29**, 1702712.
- 63 G. Yang, L. Sang, F. F. Yun, D. R. G. Mitchell, G. Casillas, N. Ye, K. See, J. Pei, X. Wang, J.-F. Li, G. J. Snyder and X. Wang, *Adv. Funct. Mater.*, 2021, **31**, 2008851.
- 64 M. Li, D. L. Cortie, J. Liu, D. Yu, S. M. K. N. Islam, L. Zhao, D. R. G. Mitchell, R. A. Mole, M. B. Cortie, S. Dou and X. Wang, *Nano Energy*, 2018, **53**, 993–1002.
- 65 L.-P. Hu, T.-J. Zhu, Y.-G. Wang, H.-H. Xie, Z.-J. Xu and X.-B. Zhao, *NPG Asia Mater.*, 2014, **6**, e88.

